JOURNAL OF SYNCHROTRON RADIATION

ISSN 1600-5775

Received 28 April 2020
Accepted 21 September 2020

Edited by A. F. Craievich, University of São Paulo, Brazil

Keywords: nanoparticles; dose enhancement; PRESAGE dosimeters; synchrotron radiation; SSRT; microbeam radiation; MRT; UV–Vis spectrophotometry.

Nanoparticle dose enhancement of synchrotron radiation in PRESAGE dosimeters

Frank M. Gagliardi,[a,b]* Rick D. Franich[c] and Moshi Geso[b]

[a]Alfred Health Radiation Oncology, The Alfred, Commercial Road, Melbourne, Victoria 3004, Australia, [b]School of Health and Biomedical Sciences, RMIT University, Plenty Road, Bundoora, Victoria 3083, Australia, and [c]School of Science, RMIT University, La Trobe Street, Melbourne, Victoria 3000, Australia.
*Correspondence e-mail: f.gagliardi@alfred.org.au

The physical absorbed dose enhancement by the inclusion of gold and bismuth nanoparticles fabricated into water-equivalent PRESAGE dosimeters was investigated. Nanoparticle-loaded water-equivalent PRESAGE dosimeters were irradiated with superficial, synchrotron and megavoltage X-ray beams. The change in optical density of the dosimeters was measured using UV–Vis spectrophotometry pre- and post-irradiation using a wavelength of 630 nm. Dose enhancement was measured for 5 nm and 50 nm monodispersed gold nanoparticles, 5–50 nm polydispersed bismuth nanoparticles, and 80 nm monodispersed bismuth nanoparticles at concentrations from 0.25 m*M* to 2 m*M*. The dose enhancement was highest for the 95.3 keV mean energy synchrotron beam (16–32%) followed by the 150 kVp superficial beam (12–21%) then the 6 MV beam (2–5%). The bismuth nanoparticle-loaded dosimeters produced a larger dose enhancement than the gold nanoparticle-loaded dosimeters in the synchrotron beam for the same concentration. For the superficial and megavoltage beams the dose enhancement was similar for both species of nanoparticles. The dose enhancement increased with nanoparticle concentration in the dosimeters; however, there was no observed nanoparticle size dependence on the dose enhancement.

1. Introduction

Synchrotron radiation therapy uses synchrotron-generated X-rays to treat tumours as an alternative to conventional radiation therapy (Blattmann *et al.*, 2005; Grotzer *et al.*, 2015). Pre-clinical studies of stereotactic synchrotron radiation therapy (SSRT) and microbeam radiation therapy (MRT) techniques demonstrate the potential of improved tumour control with increased normal-tissue sparing (Serduc *et al.*, 2009; Bräuer-Krisch *et al.*, 2015). SSRT relies on the uptake of high atomic number (Z) elements in the tumour to enhance the delivered dose to the tumour whilst MRT utilizes spatially fractionated microbeams to destroy tumour cells while sparing healthy tissue (Adam *et al.*, 2006; Renier *et al.*, 2015; Bouchet *et al.*, 2015).

The main advantages of using synchrotron-generated X-rays over conventional radiation therapy generators are the minimal beam divergence of the synchrotron beam and that ultra-high dose rates up to 16 000 Gy s^{-1} are achievable (at ESRF). The minimal beam divergence allows synchrotron X-rays to be collimated into beams with sharper penumbra than can be produced with either clinical low (kiloelectron-volt) or high (megavolt) energy machines. The ultra-high dose rates have additional advantages in terms of minimizing treatment time, and therefore intra-fractional movement, and

realizing the potential radiobiological advantages associated with FLASH radiotherapy (Bourhis *et al.*, 2019; Favaudon *et al.*, 2014).

However the fundamental problem with using low-energy synchrotron-generated X-rays, typically with a weighted mean energy on the order of 100 keV, compared with conventional radiation therapy using high-energy 6–18 MV X-rays produced by a linear accelerator, is the attenuation of the X-ray beam whilst travelling through the patient. The attenuation through tissue and bone is greater for low-energy X-rays and therefore a significant proportion of the X-rays are attenuated before reaching the target in SSRT or MRT.

Radiotherapy techniques rely on the intersection volume of multidirectional beams, having a higher dose than other irradiated tissues in the beam path(s). The steep dose fall-off for 100 keV beams means that near-surface tissues on the entry path are likely to receive high doses. This problem can be mitigated if the dose in the tumour volume can be enhanced.

The dominant interaction process in the 10–150 keV energy range is the photoelectric effect which is also highly dependent on the Z of the absorbing material. The mass attenuation coefficient for the photoelectric effect varies with Z^3. Elements with high Z have a larger X-ray absorption cross section than biological tissue in the kilovolt energy range and will therefore interact with kilovolt X-ray beams to produce photoelectrons and Auger electrons with a greater probability than biological tissue (Hossain & Su, 2012).

Whilst photoelectrons are highly energetic and travel up to hundreds of micrometres, Auger electrons have a lower energy and deposit most of their energy over a shorter range near the atom, typically less than a micrometre. If atoms with high Z are deposited in or near the cell nucleus the dose received by the cell will be enhanced by the generation of Auger electrons by the incoming X-rays.

High-Z nanoparticles (NPs) are ideal candidates to enhance the delivered dose to the tumour due to developments in the field of nanomedicine with multistage delivery systems comprised of nanovectors (Serda *et al.*, 2011). Nanovectors are nanometre-sized compounds capable of delivering NPs manufactured with biological molecules specific to tumour cells which facilitate NP uptake by the tumour and result in higher concentrations of NPs in the tumour compared with the surrounding normal tissue (Ljubimova *et al.*, 2014). Therefore, the use of high-Z NPs may enhance the dose delivered to the tumour volume without increasing the dose to healthy tissue.

Various nanovectors currently being investigated and trialled include lipid-based, polymer-based, inorganic, viral and drug conjugates providing passive targeting, active targeting and even triggered release delivery to the tumour (Tran *et al.*, 2017).

Dose enhancement has been previously reported in studies with high-Z materials and NPs *in vivo*, *in vitro* and through the use of simulations at kilovolt and megavolt energies (Rahman *et al.*, 2009; Douglass *et al.*, 2013; Lin *et al.*, 2015; Rosa *et al.*, 2017; Kuncic & Lacombe, 2018).

Increased survival times in tumour-bearing animal models have been observed for kilovolt and megavolt beams including SSRT and MRT beams when high-Z materials and NPs have been administered before radiation treatment (Hainfeld *et al.*, 2004; Adam *et al.*, 2006; Dufort *et al.*, 2016). Similarly, there is an increased inhibition of tumour cell proliferation in cell lines exposed to high-Z NPs before irradiation (Kunjachan *et al.*, 2015; Detappe *et al.*, 2016; Popovtzer *et al.*, 2016).

The reported dose enhancements vary widely for numerous reasons: the type of tumour or cell line used, NP size, shape, surface coating, concentration, and time between administration and radiation. However, after reviewing various reported NP dose enhancement factors (DEFs) (Her *et al.*, 2017; Rosa *et al.*, 2017; Kuncic & Lacombe, 2018) it is apparent that there are enhancement effects taking place other than just physical enhancement from the photoelectric effect of high-Z NPs.

Many of these experiments report the total biological dose enhancement, which consists of physical enhancement in combination with chemical and biological enhancement within cells or animal models. The total combination of enhancement may explain the variation of dose enhancement with different cell lines, NP size, shape and concentration as well as the pronounced dose enhancement even at megavolt energies where the main interaction is Compton scattering (almost independent of Z) rather than the photoelectric effect.

Chemical enhancement occurs via induced chemical sensitization of DNA to ionizing radiation and the increased formation of radicals and catalysts due to the activated surface of the NPs. If the NPs are small enough to localize in the nucleus then DNA bonds may be weakened leading to DNA damage. The NPs can also combine with molecular oxygen to generate reactive oxygen species (ROS) even without the presence of radiation. The ROS are further enhanced by radiation leading to increased cell death. Misawa & Takahashi (2011) found that the generation of ROS by 100 kVp X-rays increased with the inclusion of AuNPs. The radiosensitization increased with decreased NP size and increased NP concentration.

Biological enhancement follows from the increased ROS levels which increase the oxidative stress on cells and lead to impairment of the mitochondrial function. NPs may also interfere with cell cycle effects and inhibit radiation-induced DNA damage repair therefore making cells more sensitive to radiation (Her *et al.*, 2017). Alas, the combinations of enhancement effects contributing to the overall total biological enhancement effect are extremely difficult to separate individually; however, direct measurement of the physical dose enhancement component is achievable.

The radiochromic polyurethane dosimeter PRESAGE offers the unique opportunity to measure the physical dose enhancement effect of high-Z NPs independent of biological enhancement. PRESAGE dosimeters undergo a change in optical density (OD) upon irradiation that is proportional to dose (Adamovics & Maryanski, 2003, 2004, 2006). Refinements to the original PRESAGE formulation have resulted in dosimeters that are radiologically equivalent to water for a wide range of X-ray energies from kilovolt to megavolt (Alqathami *et al.*, 2012*a*, 2012*b*, 2015) and proton beams (Gorjiara *et al.*, 2011, 2012, 2013).

Another distinct advantage of PRESAGE over other dosimeters is that it can be fabricated to almost any desired shape or size making it suitable for a variety of analytical techniques including 1D and 2D UV–Vis spectrophotometry (Krstajić *et al.*, 2004; Youkahana *et al.*, 2016), 3D optical CT scanning (Clift *et al.*, 2010; Jackson *et al.*, 2015; Khezerloo *et al.*, 2017) and 3D high-resolution using laser scanning confocal microscopy (LSCM) (Gagliardi *et al.*, 2015).

Our previous investigations have demonstrated the radiological response of a water-equivalent (WE) PRESAGE over a range of X-ray energies (Gagliardi *et al.*, 2018*a*) as well as the dose response and stability to synchrotron-generated X-rays (Gagliardi *et al.*, 2018*b*).

In this study we investigated the response of a WE PRESAGE fabricated with and without the presence of gold and bismuth nanoparticles (AuNPs and BiNPs) over a range of energies to separate and quantify the absorbed dose enhancement due to increased energy transfer and deposition dominated by the photoelectric effect from the total biological dose enhancement effect.

2. Materials and methods

WE PRESAGE dosimeters were fabricated with the incorporation of AuNPs and BiNPs. The resultant variations in the radiological effective atomic number ($Z_{\rm eff}$) were calculated. After irradiation with three different radiation sources, the absorbed dose enhancement was quantified using UV–Vis spectroscopy of the radiochromic response.

2.1. Nanoparticle PRESAGE dosimeter fabrication

The AuNPs incorporated into PRESAGE dosimeters were monodispersed 5 nm gold 1-mercapto-(triethylene glycol) methyl ether functionalized NPs (Nanoprobes, Inc. NY, USA) and monodispersed 50 nm gold polyvinylpyrrolidone (PVP) coated nanospheres (nanoComposix, San Diego, CA, USA).

The BiNPs incorporated into PRESAGE dosimeters were polydispersed 5–50 nm bismuth sulfide polyvinylpyrrolidone coated spheres (Bi_2S_3–PVP) and monodispersed 80 nm bismuth spheres from a pure Bi metal basis of 99.9% (US Research Nanomaterials, Inc. Houston, TX, USA).

The PRESAGE dosimeters were fabricated by a method previously described (Gagliardi *et al.*, 2018*b*) using the polyurethane resin precursors Crystal Clear 204 Part A and Part B (Smooth-On Inc. Easton, PA, USA). Luecomalachite green (LMG) (Sigma–Aldrich) (2 wt%) was dissolved in Part A (48.95 wt%) and acts as the reporter compound by changing the OD of the dosimeter upon irradiation.

The NPs were incorporated by sonication using the ultrasonicator Soniclean 250T (Soniclean Pty. Ltd, Thebarton, SA, Australia) into Part B (44 wt%) for 1 h. Chloroform (Sigma–Aldrich) (5 wt%) was then added to the Part B–NP mixture to produce the free radicals required to oxidize the LMG upon irradiation. The two parts were mixed thoroughly together before the addition of the catalyst dibutyltin dilaurate (DBTDL) (Merck KGaA, Darmstadt, Germany) (0.05 wt%).

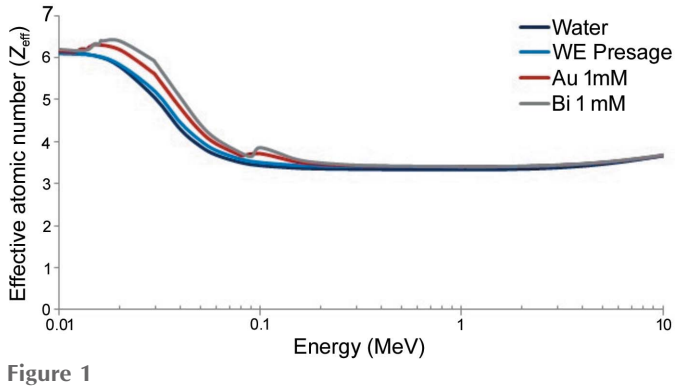

Figure 1
Radiological $Z_{\rm eff}$ based on all photon energy absorption processes (Taylor *et al.*, 2012) for water, WE PRESAGE, WE PRESAGE loaded with Au (1 m*M*) and WE PRESAGE loaded with Bi (1 m*M*).

The resultant mixture was dispensed into polymethyl methacrylate (PMMA) spectrophotometer cuvettes (12 mm × 12 mm × 45 mm) and cured for 24–48 h at 414 kPa (60 psi) pressure.

The addition of metal compounds such as DBTDL accelerates the polymerization of the polyurethane precursors, consequently reducing the curing time of the PRESAGE dosimeters, and increasing the sensitivity and the post response stability of the dosimeters (Alqathami *et al.*, 2012*a*).

The addition of DBTDL to this formulation also alters the $Z_{\rm eff}$ of the PRESAGE dosimeter to be radiologically equivalent to water over a wide range of X-ray energies (Alqathami *et al.*, 2015). Calculation of $Z_{\rm eff}$ for this formulation of PRESAGE matches the $Z_{\rm eff}$ of water within 1.7% over the effective energy range of 10 keV to 10 MeV (Gagliardi *et al.*, 2018*a*).

Using the *Auto-Zeff* software (Taylor *et al.*, 2012), which considers all of the photon energy absorption processes occurring, the $Z_{\rm eff}$ calculated for the AuNP and BiNP-loaded dosimeters at 1 m*M* concentration are shown in Fig. 1 along with that for the WE PRESAGE.

The NP-loaded dosimeters have a higher $Z_{\rm eff}$ than the WE PRESAGE in the low-energy range, with a maximum deviation of 8% for Au and 13% for Bi at 0.03 MeV (30 keV) and a deviation of 6% for Au and 10% for Bi occurring at 0.1 MeV (100 keV), which is just above the *K*-edge values for Au (80.7 keV) and Bi (90.5 keV).

Four separate batches of cuvettes were fabricated using the aforementioned method. Each batch consisted of 100 cuvettes containing 25 WE PRESAGE cuvettes to serve as the control plus 25 NP-loaded WE PRESAGE cuvettes at three different NP concentrations (Fig. 2).

2.2. Irradiations

Irradiations of the samples were performed with three X-ray sources: a clinical superficial X-ray unit, a pre-clinical synchrotron beamline and a clinical radiotherapy linear accelerator. Although significant dose enhancement is not expected at the megavolt energies of the linac, the inclusion of the 6 MV irradiation is an important control for distinguishing

Figure 2
NP-loaded WE PRESAGE filled cuvettes; (*a*) 5 nm AuNPs at 0 m*M*, 0.25 m*M*, 0.5 m*M* and 1.0 m*M*, (*b*) 50 nm AuNPs at 0 m*M*, 0.25 m*M*, 0.5 m*M* and 1.0 m*M*, (*c*) 5–50 nm BiNPs at 0 m*M*, 0.25 m*M*, 0.5 m*M* and 1.0 m*M*, (*d*) 80 nm BiNPs at 0 m*M*, 0.5 m*M*, 1.0 m*M* and 2.0 m*M*.

between (i) a genuine increase in absorbed dose due to the NPs and (ii) the possibility of a change in chemical sensitivity of the dosimeters due to the presence of metallic NPs, *i.e.* a change in the optical response per unit absorbed dose.

In each case, irradiations at each dose were conducted under well established reference conditions for delivery of the specified dose to the control cuvettes, which are therefore calibrated to dose-to-water. The NP-loaded dosimeters irradiated identically actually absorb higher doses than these due to dose enhancement. The optical change is read out and interpreted in terms of absorbed dose enhancement. The reference conditions for the three X-ray sources determined the experimental setup for the irradiations ensuring the delivered dose was at the surface of the cuvette in each setup. For the superficial X-ray unit and synchrotron beamline the reference dose is defined at the surface of the phantom and at a depth of 5 cm for the linear accelerator. The uncertainty of the delivered dose was less than 2% for all beams.

2.2.1. Superficial irradiation. The NP-loaded PRESAGE cuvettes were irradiated with 150 kVp X-rays with an HVL of 1 mm Cu on a Pantak Therapax Series3 150T SXRT machine at Alfred Health Radiation Oncology (The Alfred, Australia). To ensure reproducibility of the irradiation conditions a full scattering phantom was constructed using two 1 cm slabs of solid water attached together with a 90 mm × 90 mm × 12 mm cut-out to hold multiple cuvettes and maintain the source-to-surface distance (SSD). Fig. 3(*a*) shows two groups of four unirradiated cuvettes arranged in the phantom along with dummy cuvettes to fill the cut-out volume. A 10 cm circular applicator with a focal spot-to-surface distance (FSD) of 15 cm was positioned over the cuvettes and against the surface of the phantom [Fig. 3(*b*)] to deliver doses of 2 Gy, 5 Gy, 10 Gy and 20 Gy to the surface of the cuvettes.

2.2.2. Synchrotron irradiation. The PRESAGE cuvettes were irradiated on the Imaging and Medical Beamline (IMBL) of the Australian Synchrotron (Clayton, VIC, Australia). The synchrotron storage ring energy was 3 GeV with a ring current of 200 mA operating in top-up mode providing a constant dose rate for each irradiation. A superconducting multipole wiggler (SCMW) insertion device operating at 3.0 T in the storage ring produced a polychromatic X-ray beam that was then filtered *in vacuo* using a predetermined filter combination: (0.45 mm graphene + 21.21 mm high-density graphite + 2.83 mm Cu) referred to as

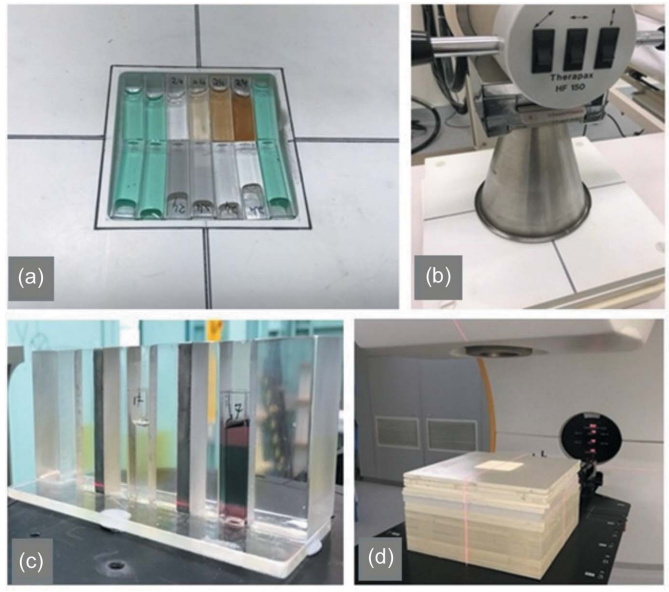

Figure 3
(*a*) Solid water phantom enclosing PRESAGE cuvettes, (*b*) setup for SXRT irradiations, (*c*) PRESAGE cuvettes in a Perspex phantom and mounted on the sample stage goniometer on the IMBL, (*d*) setup for linac irradiations.

filter set 4, F4 (Stevenson *et al.*, 2017) and *ex vacuo* filtration: (6.8 m He + 6.0 m air + 1.05 mm Be + 0.6 mm diamond + 0.15 mm Kapton + 0.114 mm Al). The resultant X-ray beam was 22 mm (W) × 2 mm (H) with a mean energy of 95.3 keV and a calculated dose rate of 275 Gy s^{-1}. The dose rate was calculated at the surface of a water phantom for the photon spectrum produced by the *in vacuo* and *ex vacuo* filtration combined with the SCMW field strength using the *spec.exe* program which has been specifically developed for the IMBL (Stevenson *et al.*, 2017).

Owing to the synchrotron beam size each cuvette was irradiated individually in a custom-made Perspex phantom attached to the sample stage goniometer for the irradiations [Fig. 3(*c*)]. The phantom was designed with sufficient size for full scattering conditions and to ensure reproducible positioning of the cuvette surface at the phantom surface. The goniometer is able to dynamically translate the phantom through the X-ray beam to produce a field size larger than 2 mm in the vertical direction. A 20 mm × 20 mm mask made

from pure tungsten (4 mm thick) was used to collimate the X-ray beam to ensure sufficient and uniform coverage across the 12 mm-wide cuvette face. The intensity of the X-ray beam decreases toward the field edges in the horizontal and vertical directions; however, the intensity of the horizontal beam is uniform to within 5% across 90% of the full width at half-maximum (FWHM) for a 20 mm × 1 mm field size (Lye *et al.*, 2016).

Each of the four NP groups had two cuvettes irradiated to 50 Gy, 100 Gy and 200 Gy for each concentration.

2.2.3. Linac irradiation. PRESAGE cuvettes were irradiated with 6 MV X-rays on a Novalis Classic (Varian Medical Systems, Palo Alto, USA) linear accelerator at Alfred Health Radiation Oncology (The Alfred, Australia). The cuvettes were placed in the solid water phantom at 5 cm depth 95 cm SSD and irradiated with 2 Gy, 5 Gy, 10 Gy, 20 Gy and 50 Gy to the surface of the cuvettes [Fig. 3(*d*)].

The dosimeters were immediately stored after irradiation in a light-free environment at −18°C to prevent any fading, post-processing or exposure to UV light and read out within 8 h after irradiation in accordance with the previously identified preferred read-out protocols (Gagliardi *et al.*, 2018*b*).

The delivered dose range was substantially higher for the synchrotron irradiations as the sample stage goniometer has an upper limit to the velocity which can translate the sample through the beam accurately to deliver low doses (less than 50 Gy) when the dose rate is 275 Gy s^{-1}. On the other hand, the range of doses delivered by the SXRT machine and linac were limited by the capacity of the machines to run for extended periods of time at the maximum dose rates of 1.112 Gy min^{-1} (SXRT) and 6 Gy min^{-1} (linac).

2.3. UV–Vis spectroscopy measurements

Optical density and absorption spectra measurements of the PRESAGE filled cuvettes were performed on a Cary 50 Spectrophotometer (Varian Inc., CA, USA) at the Australian Synchrotron. The absorption spectrum of the irradiated cuvettes with and without NPs was measured over the visible wavelength region of 500–700 nm. The wavelength of maximum absorption was 630 ± 1 nm, which is close to previously published values of 630–633 nm (Adamovics & Maryanski, 2004; Guo *et al.*, 2006; Alqathami *et al.*, 2012*b*; Gagliardi *et al.*, 2018*b*). All subsequent optical absorbance measurements were taken pre- and post-irradiation at 630 nm to determine the change in OD. The OD is defined as $\log_{10}$ of the ratio of the intensity of light passing through the sample compared with the intensity of light with no sample present, *i.e.* $OD = \log_{10}(I/I_0)$.

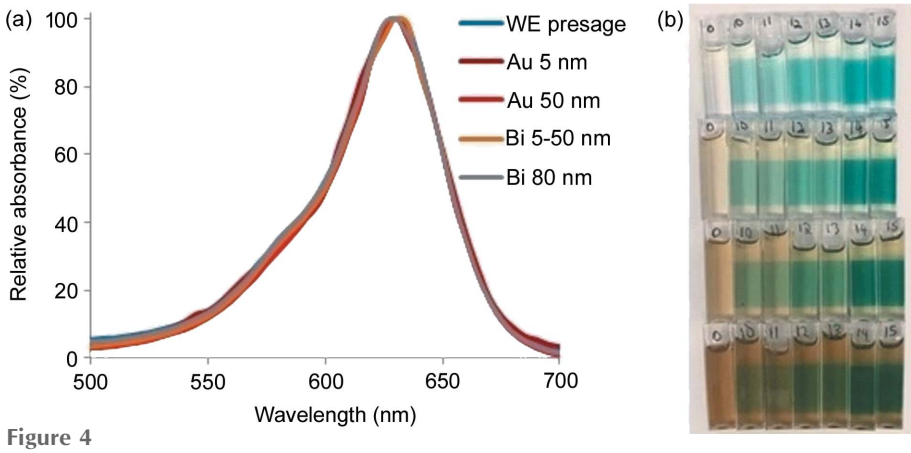

Figure 4
(*a*) Absorbance spectra of cuvettes irradiated to 200 Gy. The maximum absorption is 630 nm for the WE PRESAGE as well as AuNPs and BiNPs at 0.5 m*M*; (*b*) example of a group of irradiated cuvettes: two cuvettes irradiated to 50 Gy, 100 Gy and 200 Gy for each 5–50 nm BiNP concentration: 0 m*M*, 0.25 m*M*, 0.5 m*M* and 1.0 m*M*.

3. Results

3.1. Absorbance spectra

The absorbance spectra of the irradiated cuvettes with and without NPs displayed a maximum peak of absorption at 630 ± 1 nm (Fig. 4). The absorbance spectra were corrected using the zero-dose cuvette baseline for each NP so that the absorption from dose-proportional oxidized LMG was isolated without the absorption from the NPs or functional groups.

3.2. Dose response

Under identical irradiations to the control cuvettes, NP-loaded dosimeters showed greater increases in OD, corresponding to greater absorbed dose. The change in response gradient can be interpreted as the absorbed DEF due to the presence of high-*Z* NPs.

Fig. 5 shows the change in OD of AuNP samples (5 nm and 50 nm) for the SXRT, synchrotron and linac irradiations (150 kVp, 95.3 keV and 6 MV, respectively) for varying NP concentrations, compared with the WE PRESAGE control. Each data point is the mean of two cuvettes irradiated to the same dose with the error bars representing the difference between the two cuvettes. A fitted regression line for all eight data points in each series was plotted using a linear least-squares fitting routine which had a correlation factor $R^2 > 0.998$ for each NP series.

The change in OD of the BiNP samples (5–50 nm and 80 nm) for the three beam energies and various concentrations of NPs are compared with the WE PRESAGE controls in Fig. 6. For all NP groups there is a substantial increase of the change in OD per unit dose (*i.e.* the gradients in Figs. 5 and 6) for both the SXRT and synchrotron irradiations with only a slight increase for the linac irradiations compared with the control. The differences for different energies indicates the changing dominance of the primary interaction processes occurring within the NP-loaded dosimeters.

For the lower X-ray energies, 150 kVp and 95.3 keV, we observed an increase in the rate of change of OD compared with the control due to the strong influence of the photoelectric effect with the inclusion of high-Z NPs. At the higher energy of 6 MV the Compton effect is the dominant interaction process which is almost independent of Z and thus we observe only a small enhancement in the rate of change in OD over the control.

Importantly, the minimal gradient change for the 6 MV irradiations rules out the possibility that gradient changes might be the result of changes in chemical sensitivity of the dosimeters following the addition of NPs. Table 1 compares the rate of change of OD with respect to identical irradiations for the plotted relationships in Figs. 5 and 6.

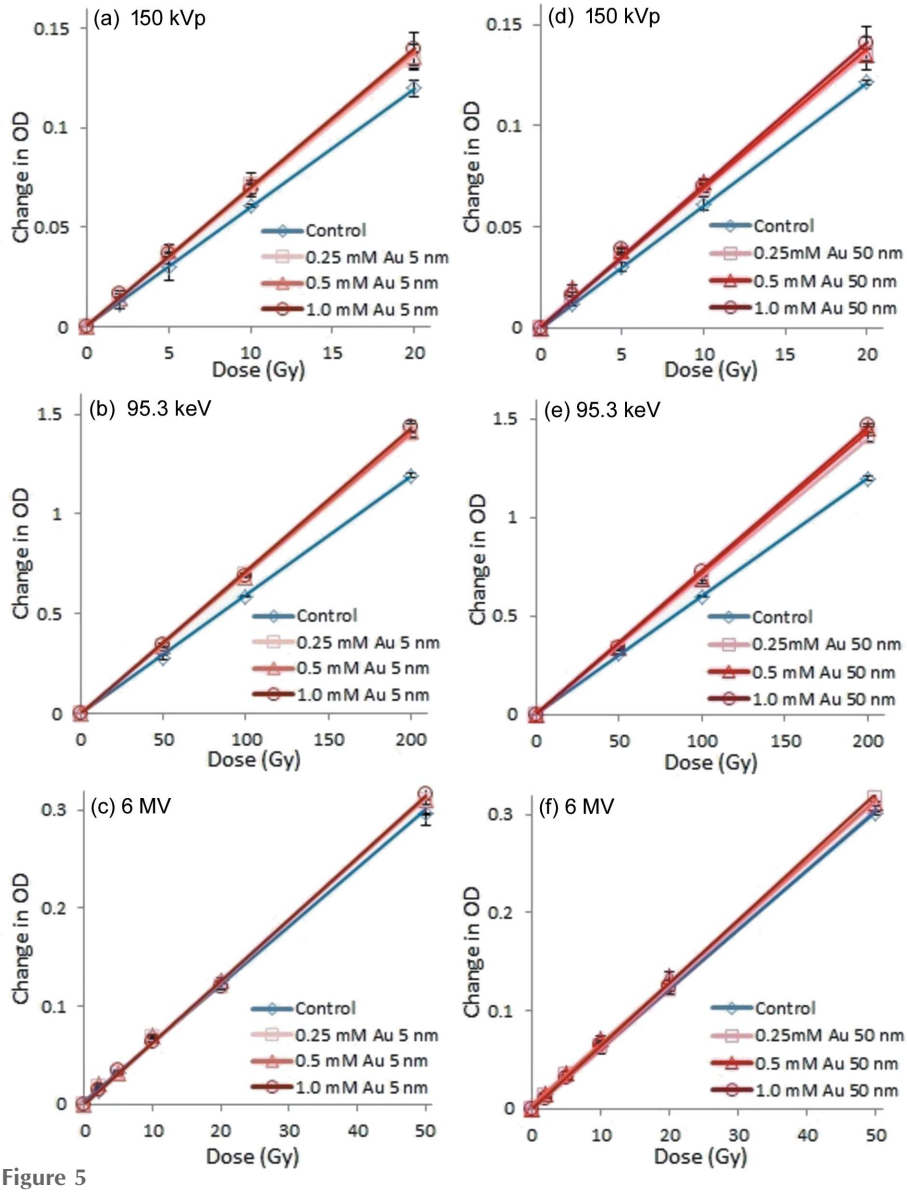

Figure 5
Change in OD as a function of delivered dose for the WE PRESAGE (control) and for 5 nm and 50 nm AuNP-loaded PRESAGE with concentrations 0.25 mM, 0.5 mM and 1.0 mM at (*a*) and (*d*) 150 kVp, (*b*) and (*e*) 95.3 keV (mean), and (*c*) and (*f*) 6 MV. The error bars represent two cuvettes of each sample type irradiated at each dose. The dose axis represents dose-to-water irradiations. The NP-loaded samples absorb more dose for the same beams/exposures.

Gradients for the control cuvettes (*i.e.* without NPs: 0 mM) represent the dose-response sensitivity of each batch of WE-PRESAGE fabricated. The typical sensitivity is approximately $\Delta OD = 6.0 \times 10^{-3}$ Gy^{-1}, with different batches ranging between 5.9×10^{-3} Gy^{-1} and 6.2×10^{-3} Gy^{-1} with a mean of $(6.0 \pm 0.1) \times 10^{-3}$ Gy^{-1}. This range in the rate of change in OD of the control dosimeters exists as each NP series was fabricated from one batch of PRESAGE with its own set of control dosimeters. Therefore, the variation in the rate of change in OD of the control dosimeters results from inter-batch variability rather than uncertainty in the gradient of the controls.

The rate of change in OD within the NP groups increased with increasing NP concentration across all energies and was highest for irradiations at 95.3 keV, followed by 150 kVp and 6 MV.

The absorbed DEF is the ratio of the gradient from NP series divided by the gradient of the control at each energy for each NP concentration. The DEF values for each NP type and concentration are listed in Table 2 and plotted in Fig. 7.

For AuNPs, the DEF ranged from 13% to 16% at 150 kVp for both NP sizes, increasing with concentration. At 95.3 keV the DEFs were higher (16% to 22%) whereas the DEFs at 6 MV were only 3% to 5%. The BiNPs displayed a similar trend, generally with higher DEFs of 12% to 21% at 150 kVp and 21% to 32% at 95.3 keV. The DEF at 6 MV was again just 2% to 5%, reflecting the decreased importance of the K-edge energy for high-energy photons. Again, differences in NP size did not make a significant difference to the DEF.

4. Discussion

The DEFs measured for AuNPs and BiNPs in PRESAGE dosimeters demonstrate the physical dose enhancement due to atomic number dependent interaction processes dominated by the photoelectric effect. Absolute dose enhancement can be seen as an increase in the gradients of the dose response curves relative to the control dosimeters irradiated with the same beams to the same number of monitor units (or beam fluence). The dose enhancement observed was 12–32% at kilovoltage energies of 150 kVp and 95.3 keV, and only 2–5% at 6 MV.

In principle, absorbed dose enhancement relative to a control dosimeter

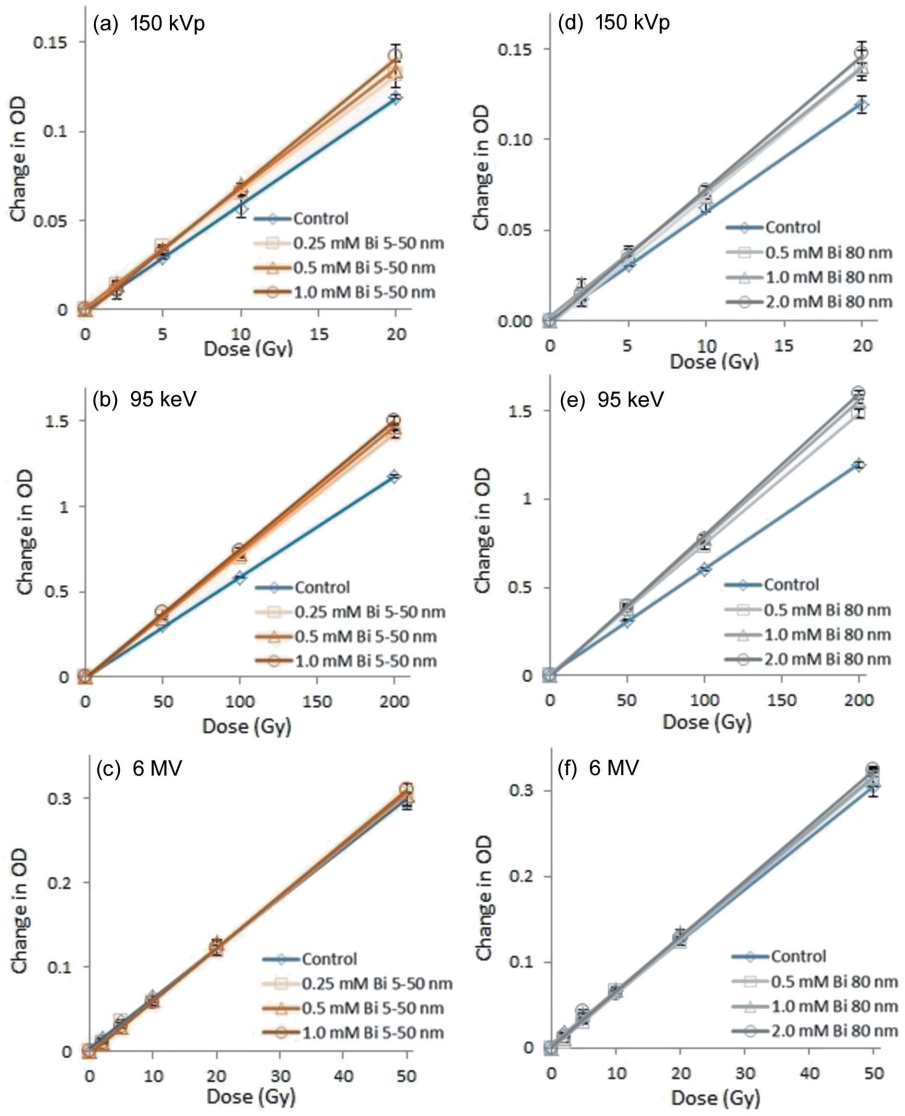

Figure 6
Change in OD as a function of delivered dose for the WE PRESAGE and for 5–50 nm BiNP-loaded PRESAGE with concentrations of 0.25 m*M*, 0.5 m*M* and 1.0 m*M*, and 80 nm BiNP-loaded PRESAGE with concentrations of 0.5 m*M*, 1.0 m*M* and 2.0 m*M* at (*a*) and (*d*) 150 kVp, (*b*) and (*e*) 95.3 keV (mean), and (*c*) and (*f*) 6 MV. The error bars represent two cuvettes of each sample type irradiated at each dose. The dose axis represents dose-to-water irradiations. The NP-loaded samples absorb more dose for the same beams.

with no NPs could be indistinguishable from a chemical sensitivity change arising from the addition of the metallic component to the WE PRESAGE. This can be understood by considering the analogy of adding more reporter compounds.

However, here we used 6 MV irradiations to demonstrate that this is not the case. If the addition of the metallic NPs altered the intrinsic sensitivity of OD to dose, then we would observe a similar increase in gradient for the NP-loaded dosimeters regardless of beam energy. Under 6 MV irradiation, where very little increase in cross section and dose enhancement is expected, we observe only a small increase consistent with the well understood minor increase in electron density and cross sections for the low-energy components of the 6 MV linac beam.

The uncertainty ranges for the DEFs were 0.01–0.03 at 150 kVp and 0.02 at 6 MV, whereas the majority of uncertainties for 95.3 keV were 0.01. The decrease in uncertainty at 95.3 keV is caused by the dose range at which the synchrotron irradiations took place, from 50 Gy to 200 Gy where the changes in OD were far greater than at 2–50 Gy, so the difference in the change in OD between two cuvettes at the same concentration irradiated to the same dose was small relative to the overall change in OD. This results in a smaller uncertainty in the gradient of the change in OD and therefore a smaller uncertainty in the DEF.

The dose enhancement was 3–12% higher for irradiations at 95.3 keV than 150 kVp. This can be explained by the relationship between the beam spectral energies and the *K*-edges for Au and Bi. The photon spectrum of the synchrotron beam with a mean energy of 95.3 keV is closer to the *K*-edge energies for Au and Bi (80.7 keV and 90.5 keV, respectively) than the 150 kVp SXRT beam which has a mean energy of approximately 50–75 keV. The synchrotron beam also has a greater fraction of its spectral fluence above the *K*-edges.

The DEFs were greater for BiNPs than for AuNPs at 95.3 keV; however, at 150 kVp and 6 MV the DEFs were similar within experimental uncertainties. The dose enhancement at the kiloelectronvolt energies was approximately 5–6 times higher than at 6 MV for both AuNPs and BiNPs due to the reduced significance of proximity to the *K*-edge energies.

Comparison of measured DEFs with other published results reveals a wide variety of systems including NP compounds and sizes, beam energies and spectra. This makes direct comparison complex. Alqathami *et al.* (2016) found that the dose enhancement for 50 nm Bi_2O_3NPs and 50 nm AuNPs at concentrations of 0.5 m*M* were also on the order of 5–6 times higher with a SXRT 100 kVp beam compared with 6 MV in the PRESAGE dosimeters that were fabricated with a bromine-based radical initiator.

The measured dependence observed in the present work is much more modest than the DEFs at 100 kVp reported by Alqathami *et al.* (2016) of 1.77 for AuNPs and 1.90 for BiNPs at 0.50 m*M* concentration. The difference in magnitude of the DEFs arises from two possible causes: (i) a lower value of the

Table 1
Gradients of the fitted regression lines in Figs. 5 and 6 [(ΔOD) $\times 10^{-3}$ Gy^{-1}].

The uncertainty is the statistically derived standard error of the gradient of the fitted regression line rounded to one significant figure.

		Energy		
Nanoparticle	Concentration (m*M*)	150 kVp (±0.1)	95.3 keV (mean) (±0.1)	6 MV (±0.1)
Au 5 nm	0	6.0	5.9	6.0
	0.25	6.8	7.0	6.2
	0.5	6.9	7.0	6.2
	1	7.0	7.1	6.3
Au 50 nm	0	6.1	6.0	6.1
	0.25	6.8	7.0	6.3
	0.5	6.9	7.2	6.4
	1	7.1	7.3	6.4
Bi 5–50 nm	0	5.9	5.9	5.9
	0.25	6.6	7.1	6.1
	0.5	6.8	7.3	6.1
	1	7.0	7.5	6.2
Bi 80 nm	0	6.0	6.0	6.2
	0.5	7.0	7.4	6.3
	1	7.1	7.8	6.4
	2	7.3	7.9	6.5

control gradient of 0.0055 Gy^{-1} given by the authors in that work, which is noticeably lower than their previously reported PRESAGE dosimeters fabricated with a bromine-based radical initiator of 0.0089 Gy^{-1} (Alqathami *et al.*, 2012*b*) and 0.016 Gy^{-1} (Alqathami *et al.*, 2013); and (ii) the 100 kVp X-ray beam reported in that work is not comparable with the 95.3 keV(mean) synchrotron beam or the 150 kVp beam in our work. The 100 kVp X-ray tube beam has a higher percentage of the spectrum well below the *K*-edge energies of Au and Bi

Table 2
The dose enhancement factor at each energy and concentration for the AuNPs and BiNPs.

The stated uncertainty is the quadrature sum of the uncertainties of the two gradients forming the ratio.

		Energy		
Nanoparticle	Concentration (m*M*)	150 kVp (±0.01–0.03)	95.3 keV (mean) (±0.01–0.02)	6 MV (±0.02)
Au 5 nm	0.25	1.13	1.18	1.03
	0.5	1.15	1.18	1.03
	1	1.16	1.20	1.04
Au 50 nm	0.25	1.13	1.16	1.03
	0.5	1.14	1.19	1.04
	1	1.16	1.22	1.05
Bi 5–50 nm	0.25	1.12	1.21	1.03
	0.5	1.15	1.24	1.04
	1	1.18	1.28	1.05
Bi 80 nm	0.5	1.15	1.24	1.02
	1	1.17	1.29	1.03
	2	1.21	1.32	1.05

where the deviation in the radiological Z_{eff} compared with PRESAGE is larger than for the synchrotron beam (Fig. 1).

Taha *et al.* (2018) used Monte Carlo (MC) simulations to assess the dose enhancement in a tumour model by the addition of Bi_2O_3NPs with low-energy (34.4 keV) X-rays from a ^{131}Cs source. The reported dose enhancement to the tumour compared with the tumour without NPs was 18.55 times greater at a relatively high concentration of 70 mg g^{-1} Bi_2O_3NPs (350 m*M*) in the tumour and 2 times greater at 5 mg g^{-1} Bi_2O_3NPs (25 m*M*) in the tumour. The maximum BiNP concentration used in our study was 2 m*M*, which equates to 0.4 mg g^{-1}.

Several studies have reported DEFs of AuNPs and BiNPs that increase with NP concentration in PRESAGE dosimeters (Alqathami *et al.*, 2016) and MC simulations for SXRT energies (Hossain & Su, 2012; Zheng & Chow, 2017). We observed an overall increase in the DEFs with concentration at megavolt SXRT as well as synchrotron energies for both AuNPs and BiNPs, although the increase in DEF was not linear with NP concentration (Fig. 7). This non-linear relationship has also been reported for AuNPs and BiNPs in PRESAGE dosimeters (Alqathami *et al.*, 2016) where a fivefold increase in concentration only resulted in a 70% increase in the DEF.

When studying the measured dose enhancement increase with NP concentration, one limitation of our experimental configuration using UV–Vis spectrophotometry with NP-loaded PRESAGE dosimeters is the absolute value of the OD of the dosimeter before (and therefore after) irradiation. As the NP concentration increases, so does the

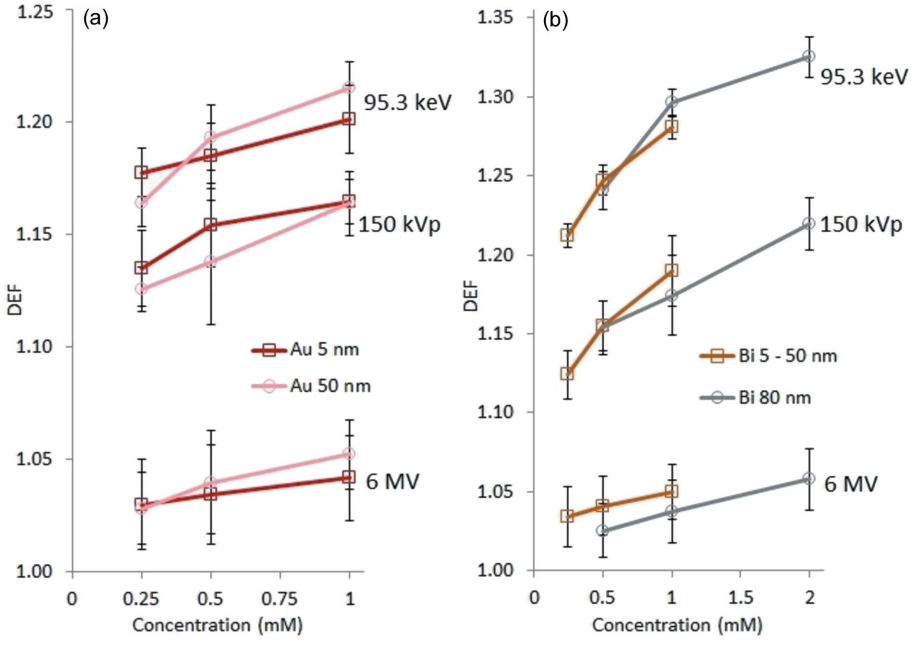

Figure 7
DEF versus NP concentration for (*a*) AuNPs and (*b*) BiNPs at 150 kVp, 95.3 keV (mean) and 6 MV. Error bars represent the total uncertainty in the DEF (see Table 2).

OD of the unirradiated dosimeters – the upper absorbance limit of the spectrophotometer [3.3 absorbance units (AU)] may be reached before irradiation. Therefore, any change in OD above this value would not be measureable, which in turn places an upper limit on NP concentrations that can be studied with this experimental configuration. Clinically relevant concentrations can be studied however, and optical saturation was not observed in any of our measurements (see Figs. 5 and 6). Measured dose enhancements achievable for the synchrotron beam were 20–22% for 1 m*M* AuNPs and 28–32% for 1 m*M* and 2 m*M* BiNPs. When considering the importance of toxicity of NPs, these concentrations are clinically relevant. The limit of optical saturation at higher NP concentrations could be overcome in future work by optimizing the experimental configuration using cuvettes with a shorter path length, reducing the irradiated volume using a synchrotron microbeam (Doran *et al.*, 2017) or by using an alternative readout wavelength which is not at the peak of the LMG absorption curve.

There was no discernible difference in the DEF with NP size for either AuNPs or BiNPs implying that the dose enhancement of NPs is not size dependent between 5 nm and 80 nm or that our investigation using PRESAGE dosimeters is not sensitive enough to observe a small size dependence on the dose enhancement if it exists.

The dose enhancement measured in our PRESAGE dosimeters was greater at kilovolt energies than at 6 MV which had maximum DEF of 1.05; however, *in vitro* studies with various cell lines and AuNPs of different size and surface coating have demonstrated larger effects on cell viability at 6 MV of 1.59–1.86 along with even larger effects at kilovolt energies (Wang *et al.*, 2015; Liu *et al.*, 2008).

The reported high-dose enhancement at 6 MV observed in cells *in vitro* should therefore be considered as the total biological effect enhancement as the absorbed dose enhancement due to increased energy deposition is not expected to be this significant. The total biological effect enhancement is a combination of the absorbed dose increase plus chemical and biological enhancement all contributing to the radiosensitization.

An understanding of the individual contributions from these processes, and their dependence on NP concentration, is important. Previous studies (discussed in detail below) have shown biological effect enhancement by NPs that exceeds the factor explained by absorbed dose increase alone. Significant dependence on NP composition, size and shape have been observed and attributed to chemical and biological processes – the most significant of which is cellular uptake. This is tantamount to influencing the NP concentrations being achieved. For detailed discussion on cellular uptake efficiency due to the size, shape and surface coating of NPs, refer to the works by Butterworth *et al.* (2012), Chithrani *et al.* (2006, 2010), Wang *et al.* (2013), Xie *et al.* (2017) and Wolfe *et al.* (2015).

The reported *in vitro* and *in vivo* studies for clinical X-ray beams suggest that a further increase in the total biological dose enhancement is also possible for synchrotron beams. The consideration of chemical and biological enhancements in cells and animal models for synchrotron beams is likely to raise the total effect above the physical absorbed dose only enhancements of 20–32% in our results. Dose enhancements above 20–32% could significantly improve the dose delivery to the target volume at depth, where the synchrotron beam (95.3 keV average) is approximately attenuated by a factor of two at a depth of 50 mm and a factor of five at a depth of 100 mm in a water phantom (Gagliardi *et al.*, 2018*b*), and greater if the synchrotron beam traverses tissue and bone before reaching the target volume. Beam hardening of the X-ray beam with depth through tissue and bone may also influence the physical dose enhancement at the target volume due to an increase in the average X-ray beam energy.

Increasing the concentration of NPs increases the absorbed dose; however, there is a limit to the concentration of NPs that can be loaded into PRESAGE cuvettes due to the OD rendering the sample too opaque to read out using UV–Vis spectrophotometry. This is a limitation on the use of PRESAGE to measure the DEF, not a saturation of the achievable absorbed dose increase. Higher concentrations of NPs may increase the absorbed dose further; however, the toxicity to living organisms must be considered.

When contemplating the use of NPs for dose enhancement for clinical trials it must be noted that the use in animal and human models is only possible if the NPs are biocompatible as properties of NPs differ widely from the inert metallic form. Nanovectors employed to deliver NPs and facilitate preferential uptake by the tumour must not be toxic to the subject, thus rendering the enhancement of dose to the tumour futile if toxic side effects to the healthy tissue are greater (Yildirimer *et al.*, 2011).

Several studies have reviewed the toxicity of AuNPs and BiNPs *in vitro* (Naha *et al.*, 2015; Yan-Peng *et al.*, 2017; Deng *et al.*, 2017; Lopez-Chaves *et al.*, 2018; Abudayyak *et al.*, 2017). The impact of NP size, shape, type of conjugate, administration route and immunological response with different cell lines can vary widely. The cytotoxicity generally increases with concentration; however, the cytocompatibility of Au and Bi remains high due to the available choice of size, shape and conjugates available.

Hainfeld *et al.* (2011) found the 50% lethal dose or the dose that kills 50% of the animals (LD50) for 11 nm AuNPs was >5 g Au per kg when injected into mice; however, significant dose enhancement was observed for mice injected at concentrations lower than the LD50 of 2.7 g and 4 g Au per kg (Hainfeld *et al.*, 2004; Hainfeld *et al.*, 2013). Dose enhancement *in vitro* has been reported at concentrations of 0.25–1 m*M* for Au which equates to approximately 0.25–1 g Au l^{-1} (Rahman *et al.*, 2009) which is lower than the LD50 of AuNPs by a factor of 5. The concentrations of NPs used in this study were also all considerably lower than the LD50 of AuNPs in mice by a factor of approximately five, thus the concentrations studied here are clinically relevant.

The physical absorbed dose enhancement by synchrotron radiation may possibly be increased even further if a monochromatic synchrotron beam was used at the optimum energies for dose enhancement with AuNPs and/or BiNPs. In this

study a polychromatic spectrum typical of MRT was used as a preliminary investigation to the physical dose enhancement effects of NPs on synchrotron-generated microbeam arrays.

5. Conclusions

The physical absorbed dose enhancements of AuNP and BiNP have been measured in NP-loaded PRESAGE dosimeters. The increase in dose was up to 22% for 5 nm and 50 nm AuNPs at 1 m*M* concentration irradiated in a 95.3 keV mean energy synchrotron beam and 16% in a 150 kVp SXRT beam. Similarly for BiNPs, the increase in dose was up to 32% for 5–50 nm (polydisperse) and 80 nm BiNPs irradiated in a 95.3 keV mean energy synchrotron beam and 21% in a 150 kVp SXRT beam at concentrations up to 2 m*M*. The increase in dose for 6 MV irradiations for both AuNPs and BiNPs only reached a maximum of 5%.

At similar concentrations, the dose enhancement caused by the presence of NPs was higher for Bi than for Au in the synchrotron beam and similar in the SXRT beam. The absorbed dose enhancement due to X-ray interactions was higher at kilovolt than megavolt energies and was not dependent on the size of the NP. The absorbed dose enhancement increased with NP concentration; however, the increase in DEF is not linear with NP concentration. This reflects the decreasing efficiency of the interaction for the additional energy deposited. The achievable absorbed dose enhancement will also be constrained by cellular uptake and cellular toxicity. Therefore there is a practical limit to the amount of physical dose enhancement possible. Future experiments with cell and animal models should consider not only the uptake efficiency to increase concentration but the biological and chemical enhancements possible due to the size, shape and surface coating of NPs which, along with the absorbed dose enhancement measured here, contribute significantly to the total biological effect enhancement.

Acknowledgements

We would also like to acknowledge the Australian Synchrotron and ANSTO for providing experimental time on the IMBL beamline, and the IMBL beamline scientists for their technical assistance.

Funding information

The authors were grateful for financial assistance from J. Millar and T. Ackerly (Alfred Health Radiation Oncology, Alfred Health), the Australian Government Research Training Program Scholarship and the Joint Research Engagement (JRE) Engineering Cadetship.

References

Abudayyak, M., Öztaş, E., Arici, M. & Özhan, G. (2017). *Chemosphere*, **169**, 117–123.
Adam, J. F., Joubert, A., Biston, M. C., Charvet, A. M., Peoc'h, M., Le Bas, J. F., Balosso, J., Estève, F. & Elleaume, H. (2006). *Int. J. Radiat. Oncol. Biol. Phys.* **64**, 603–611.
Adamovics, J. & Maryanski, M. J. (2003). *Med. Phys.* **30**, 1349.
Adamovics, J. & Maryanski, M. J. (2004). *J. Phys. Conf. Ser.* **3**, 172–175.
Adamovics, J. & Maryanski, M. J. (2006). *Rad. Prot. Dosim.* **120**, 107–112.
Alqathami, M., Adamovics, J., Benning, R., Qiao, G., Geso, M. & Blencowe, A. (2013). *Radiat. Phys. Chem.* **85**, 204–209.
Alqathami, M., Blencowe, A., Geso, M. & Ibbott, G. (2015). *Radiat. Meas.* **74**, 12–19.
Alqathami, M., Blencowe, A., Geso, M. & Ibbott, G. (2016). *J. Biomed. Nanotechnol.* **12**, 464–471.
Alqathami, M., Blencowe, A., Qiao, G., Adamovics, J. & Geso, M. (2012*a*). *Radiat. Phys. Chem.* **81**, 1688–1695.
Alqathami, M., Blencowe, A., Qiao, G., Butler, D. & Geso, M. (2012*b*). *Radiat. Phys. Chem.* **81**, 867–873.
Blattmann, H., Gebbers, J. O., Bräuer-Krisch, E., Bravin, A., Le Duc, G., Burkard, W., Di Michiel, M., Djonov, V., Slatkin, D. N., Stepanek, J. & Laissue, J. A. (2005). *Nucl. Instrum. Methods Phys. Res. A*, **548**, 17–22.
Bouchet, A., Serduc, R., Laissue, J. A. & Djonov, V. (2015). *Phys. Med.* **31**, 634–641.
Bourhis, J., Montay-Gruel, P., Gonçalves Jorge, P., Bailat, C., Petit, B., Ollivier, J., Jeanneret-Sozzi, W., Ozsahin, M., Bochud, F., Moeckli, R., Germond, J. F. & Vozenin, M. C. (2019). *Radiother. Oncol.* **139**, 11–17.
Bräuer-Krisch, E., Adam, J.-F., Alagoz, E., Bartzsch, S., Crosbie, J., DeWagter, C., Dipuglia, A., Donzelli, M., Doran, S., Fournier, P., Kalef-Ezra, J., Kock, A., Lerch, M., McErlean, C., Oelfke, U., Olko, P., Petasecca, M., Povoli, M., Rosenfeld, A., Siegbahn, E. A., Sporea, D. & Stugu, B. (2015). *Phys. Med.* **31**, 568–583.
Butterworth, K. T., McMahon, S. J., Currell, F. J. & Prise, K. M. (2012). *Nanoscale*, **4**, 4830–4838.
Chithrani, B. D., Ghazani, A. A. & Chan, W. C. W. (2006). *Nano Lett.* **6**, 662–668.
Chithrani, D. B., Jelveh, S., Jalali, F., van Prooijen, M., Allen, C., Bristow, R. G., Hill, R. P. & Jaffray, D. A. (2010). *Radiat. Res.* **173**, 719–728.
Clift, C., Thomas, A., Adamovics, J., Chang, Z., Das, I. & Oldham, M. (2010). *Phys. Med. Biol.* **55**, 1279–1293.
Deng, J., Yao, M. & Gao, C. (2017). *Acta Biomater.* **53**, 610–618.
Detappe, A., Kunjachan, S., Sancey, L., Motto-Ros, V., Biancur, D., Drane, P., Guieze, R., Makrigiorgos, G. M., Tillement, O., Langer, R. & Berbeco, R. (2016). *J. Controlled Release*, **238**, 103–113.
Doran, S. J., Pellicioli, P., Adamovics, J. & Brauer-Krisch, E. (2017). *J. Phys. Conf. Ser.* **847**, 012028.
Douglass, M., Bezak, E. & Penfold, S. (2013). *Med. Phys.* **40**, 071710.
Dufort, S., Le Duc, G., Salomé, M., Bentivegna, V., Sancey, L., Bräuer-Krisch, E., Requardt, H., Lux, F., Collect, J. L., Perriat, P., Roux, S. & Tillement, O. (2016). *Sci. Rep.* **6**, 29678.
Favaudon, V., Caplier, L., Monceau, V., Pouzoulet, F., Sayarath, M., Fouillade, C., Poupon, M. F., Brito, I., Hupé, P., Bourhis, J., Hall, J., Fontaine, J. J. & Vozenin, M. C. (2014). *Sci. Transl. Med.* **6**, 245ra93.
Gagliardi, F. M., Cornelius, I., Blencowe, A., Franich, R. D. & Geso, M. (2015). *Med. Phys.* **42**, 6973–6986.
Gagliardi, F. M., Day, L., Poole, C. M., Franich, R. D. & Geso, M. (2018*a*). *Med. Phys.* **45**, 1255–1265.
Gagliardi, F. M., Franich, R. D. & Geso, M. (2018*b*). *Phys. Med. Biol.* **63**, 235027.
Gorjiara, T., Hill, R., Kuncic, Z., Adamovics, J., Bosi, S., Kim, J.-H. & Baldock, C. (2011). *Med. Phys.* **38**, 2265–2274.
Gorjiara, T., Kacperek, A., Kuncic, Z., Baldock, C. & Doran, S. (2013). *J. Phys. Conf. Ser.* **444**, 012058.
Gorjiara, T., Kuncic, Z., Doran, S., Adamovics, J. & Baldock, C. (2012). *Med. Phys.* **39**, 7071–7079.
Grotzer, M. A., Schültke, E., Bräuer-Krisch, E. & Laissue, J. A. (2015). *Phys. Med.* **31**, 564–567.
Guo, P. Y., Adamovics, J. A. & Oldham, M. (2006). *Med. Phys.* **33**, 1338–1345.

Hainfeld, J. F., O'Connor, M. J., Dilmanian, F. A., Slatkin, D. N., Adams, D. J. & Smilowitz, H. M. (2011). *Br. J. Radiol.* **84**, 526–533.
Hainfeld, J., Slatkin, D. & Smilowitz, H. (2004). *Phys. Med. Biol.* **49**, N309–N315.
Hainfeld, J. F., Smilowitz, H. M., O'Connor, M. J., Dilmanian, F. A. & Slatkin, D. N. (2013). *Nanomedicine*, **8**, 1601–1609.
Her, S., Jaffray, D. A. & Allen, C. (2017). *Adv. Drug. Deliv. Rev.* **109**, 84–101.
Hossain, M. & Su, M. (2012). *J. Phys. Chem. C*, **116**, 23047–23052.
Jackson, J., Juang, T., Adamovics, J. & Oldham, M. (2015). *Phys. Med. Biol.* **60**, 2217–2230.
Khezerloo, D., Nedaie, H. A., Farhood, B., Zirak, A., Takavar, A., Banaee, N., Ahmadalidokht, I. & Kron, T. (2017). *J. Can. Res. Ther.* **13**, 419–424.
Krstajić, N., Wai, P., Adamovics, J. & Doran, S. (2004). *J. Phys. Conf. Ser.* **3**, 244–247.
Kuncic, Z. & Lacombe, S. (2018). *Phys. Med. Biol.* **63**, 02TR1.
Kunjachan, S., Detappe, A., Kumar, R., Ireland, T., Cameron, L., Biancur, D. E., Motto-Ros, V., Sancey, L., Sridhar, S., Makrigiorgos, G. M. & Berbeco, R. I. (2015). *Nano Lett.* **15**, 7488–7496.
Lin, Y., Paganetti, H., McMahon, S. J. & Schuemann, J. (2015). *Med. Phys.* **42**, 5890–5902.
Liu, C.-J., Wang, C.-H., Chien, C.-C., Yang, T.-Y., Chen, S.-T., Leng, W.-H., Lee, C.-F., Lee, K.-H., Hwu, Y., Lee, Y.-C., Cheng, C.-L., Yang, C.-S., Chen, Y. J., Je, J. H. & Margaritondo, G. (2008). *Nanotechnology*, **19**, 295104.
Ljubimova, J. Y., Ding, H., Portilla-Arias, J., Patil, R., Gangalum, P. R., Chesnokova, A., Inoue, S., Rekechenetskiy, A., Nassoura, T., Black, K. L. & Holler, E. (2014). *J. Vis. Exp.* **88**, e50668.
Lopez-Chaves, C., Soto-Alvaredo, J., Montes-Bayon, M., Bettmer, J., Llopis, J. & Sanchez-Gonzalez, C. (2018). *Nanomedicine*, **14**, 1–12.
Lye, J. E., Harty, P. D., Butler, D. J., Crosbie, J. C., Livingstone, J., Poole, C. M., Ramanathan, G., Wright, T. & Stevenson, A. W. (2016). *Phys. Med. Biol.* **61**, 4201–4222.
Misawa, M. & Takahashi, J. (2011). *Nanomedicine*, **7**, 604–614.
Naha, P. C., Chhour, P. & Cormode, D. P. (2015). *Toxicol. In Vitro*, **29**, 1445–1453.
Popovtzer, A., Mizrachi, A., Motiei, M., Bragilovski, D., Lubimov, L., Levi, M., Hilly, O., Ben-Aharon, I. & Popovtzer, R. (2016). *Nanoscale*, **8**, 2678–2685.
Rahman, W. N. B. N., Ackerly, T., He, C. F., Jackson, P., Wong, C., Davidson, R. & Geso, M. (2009). *Nanomedicine*, **5**, 136–142.
Renier, M., Adam, J.-F., Nemoz, C., Brochard, T., Berkvens, P., Bravin, A., Berruyer, G., Elleaume, H., Balosso, J., Le Bas J.-F. & Estève, F. (2015). *Proceedings of the 8th Medical Applications of Synchrotron Radiation Conference (MASR2015)*, 5–8 October 2015, Villard de Lans, France.
Rosa, S., Connolly, C., Schettino, G., Butterworth, K. T. & Prise, K. M. (2017). *Nanotechnology*, **8**, 2.
Serda, R. E., Godin, B., Blanco, E., Chiappini, C. & Ferrari, M. (2011). *Biochim. Biophys. Acta*, **1810**, 317–329.
Serduc, R., Bräuer-Krisch, E., Bouchet, A., Renaud, L., Brochard, T., Bravin, A., Laissue, J. & Le Duc, G. (2009). *J. Synchrotron Rad.* **16**, 587–590.
Stevenson, A. W., Crosbie, J. C., Hall, C. J., Häusermann, D., Livingstone, J. & Lye, J. E. (2017). *J. Synchrotron Rad.* **24**, 110–141.
Taha, E., Djouider, F. & Banoqitah, E. (2018). *Eng. Sci. Med.* **41**, 363–370.
Taylor, M. L., Smith, R. L., Dossing, F. & Franich, R. D. (2012). *Med. Phys.* **39**, 1769–1778.
Tran, S., DeGiovanni, P.-J., Piel, B. R. P. & Rai, P. (2017). *Ca. Nanomedicine: Rev. Recent. Success Drug. Deliv. Clin. Transl. Med.* **6**, 44.
Wang, C., Jiang, Y., Li, X. & Hu, L. (2015). *Breast Cancer*, **22**, 413–420.
Wang, Y., Black, K. C. L., Luehmann, H., Li, W., Zhang, Y., Cai, X., Wan, D., Liu, S.-Y., Li, M., Kim, P., Li, Z.-Y., Wang, L. V., Liu, Y. & Xia, Y. (2013). *ACS Nano*, **7**, 2068–2077.
Wolfe, T., Chatterjee, D., Lee, J., Grant, J. D., Bhattarai, S., Tailor, R., Goodrich, G., Nicolucci, P. & Krishnan, S. (2015). *Nanomedicine*, **11**, 1277–1283.
Xie, X., Liao, J., Shao, X., Li, Q. & Lin, Y. (2017). *Sci. Rep.* **7**, 3827.
Yan-Peng, J., Bu-Yun, M., Xia-Wei, W. & Zhi-Yong, Q. (2017). *Chin. Chem. Lett.* **28**, 691–702.
Yildirimer, L., Thanh, N. T. K., Loizidou, M. & Seifalian, A. M. (2011). *Nano Today*, **6**, 585–607.
Youkahana, E. Q., Gagliardi, F. M. & Geso, M. (2016). *Biomed. Phys. Eng. Express.* **2**, 045009.
Zheng, X. J. & Chow, J. C. L. (2017). *J. Radiol.* **9**, 63–71.